JOURNAL OF Materials CHEMISTRY

Structural and electrochemical properties of Li(Fe, Co)$_x$Mn$_{2-x}$O$_4$ solid solution as 5 V positive electrode materials for Li secondary batteries

Hikari Shigemura,[a,b]† Mitsuharu Tabuchi,*[a] Hironori Kobayashi,[a] Hikari Sakaebe,[a] Atsushi Hirano[c] and Hiroyuki Kageyama[a]

[a]*Special Division of Green Life Technology, National Institute of Advanced Industrial Science and Technology (AIST), Osaka 563-8577, Japan. E-mail: m-tabuchi@aist.go.jp*
[b]*New Energy and Industrial Technology Development Organization (NEDO), Tokyo 170-0013, Japan*
[c]*Faculty of Engineering, Mie University, Mie 514-8507, Japan*

Received 18th January 2002, Accepted 20th March 2002
First published as an Advance Article on the web 19th April 2002

Solid solutions, Li(Fe, Co)$_x$Mn$_{2-x}$O$_4$ ($0 \leqslant x \leqslant 0.5$ for Fe, $0 \leqslant x \leqslant 1.0$ for Co) were synthesized by solid state reaction at 1023–1073 K in O_2 atmosphere. The compositional dependence of lattice parameters and cation distribution was studied by neutron diffraction Rietveld refinement. It was revealed that Fe and Co partially occupied tetrahedral 8a sites and the 1 : 3 and 1 : 1 ordering did not occur on Fe (Co) and Mn ions in octahedral 16d sites. X-Ray absorption fine structure (XAFS) analysis showed the variation of valences and metal–oxygen interatomic distances of Mn, Fe, and Co. The Fe–O distance was longer whereas the Co–O distance was shorter compared to the averaged M_{16d}–O_{32e} distance calculated from the lattice parameters. Charge and discharge properties were studied in voltage range 3.0–5.3 V *vs.* Li/Li$^+$.

Introduction

Lithium manganese spinel, $LiMn_2O_4$, is a candidate for an advanced 4 V positive electrode material for lithium batteries and lithium ion batteries. Since it has economical and environmental advantages over commercially successful $LiCoO_2$ and highly potential $LiNiO_2$, the electrochemical characteristics of $LiMn_2O_4$ have been widely investigated for use in portable electronic devices and zero emission vehicles. The stoichiometric $LiMn_2O_4$, however, exhibits a high capacity fading on cycling because of the strong Jahn–Teller distortion of trivalent Mn and so on. The cyclability is improved by replacing a small part of Mn with Li or other metals (Mg, Cr, Co, and Ni) in order to raise the average valence of Mn over 3.5+.[1,2] New plateaus also appear over 4.5 V *vs.* Li/Li$^+$ instead of capacity loss at a 4 V plateau when some transition metals (M = Cr,[3] Fe,[4] Co,[5] Ni,[6] and Cu[7]) are substituted to $LiMn_2O_4$. Kawai *et al.* reported the electrochemical properties of $LiCo_xMn_{2-x}O_4$ ($0 \leqslant x \leqslant 1$)[5] and $LiFe_{0.5}Mn_{1.5}O_4$.[4] The $LiCo_xMn_{2-x}O_4$ solid solutions operate at 4.0 and 5.1 V, and the 5.1 V plateau monotonously increases in capacity with increasing x. $LiFe_{0.5}Mn_{1.5}O_4$ showed two plateaus centered at 4.0 and 5.0 V, whose capacities are *ca.* 70 mAh g^{-1} each. Recently we reported the structural and electrochemical properties of $LiFe_xMn_{2-x}O_4$ ($0 \leqslant x \leqslant 0.5$) and the charge and discharge mechanism.[8] It was revealed from *in-situ* ^{57}Fe Mössbauer spectroscopy measurements that the redox couple of Fe3+/4+ contributed to the 5 V capacity.

$LiMn_2O_4$ spinel possesses a cubic symmetry with space group $Fd\bar{3}m$. The oxygen ions form a cubic close packed array occupying 32e sites; manganese ions occupy half of the octahedral sites, 16d, forming a three dimensional framework of edge-sharing MnO_6 octahedra; and lithium ions occupy one-eighth of the tetrahedral interstices, 8a sites. In $LiM_xMn_{2-x}O_4$ (M = transition metal), M atoms can occupy 16d sites, substituting for Mn, and/or 8a sites, substituting for Li. Neutron diffraction (ND) measurement is useful to study such cation distribution, because Li and O have detectable atomic scattering factors and transition metals are more easily differentiated compared with X-ray diffraction. In $LiCr_xMn_{2-x}O_4$ ($x \leqslant 0.33$), ND refinement revealed that Cr substituted on 16d sites selectively and that Li occupied only 8a sites.[9] ND measurement also gives information about the ordering of Mn and M on 16d sites: a 1 : 3 order for $(Li)_{8a}[M_{0.5}Mn_{1.5}]_{16d}O_4$ and a 1 : 1 order for $(Li)_{8a}[M_{1.0}Mn_{1.0}]_{16d}O_4$. The 1 : 3 order on 16d sites was observed in $LiCu_{0.5}Mn_{1.5}O_4$, giving additional reflections which indexed on a primitive cubic cell ($P4_332$) instead of $Fd\bar{3}m$ in the ND pattern.[10] The information of local and electronic structure around a selected absorbing atom can be obtained by X-ray absorption fine structure (XAFS) analysis. There are some studies using this technique concerned with compositional dependence of valence and local structure around electrochemically active ions, and with the changes during charge and discharge processes in $LiM_xMn_{2-x}O_4$ (M = Co,[11] Cr,[12] and Ni[13]). In the present paper, we report on the structural properties using ND and XAFS analysis and on the magnetic and electrochemical properties for Fe- or Co-substituted $LiMn_2O_4$.

Experimental

Solid solutions of $LiFe_xMn_{2-x}O_4$ (x = 0, 0.1, 0.3, 0.5) and $LiCo_xMn_{2-x}O_4$ (x = 0.5, 1.0) were prepared from $MnCO_3$, FeOOH, Co_3O_4, and $LiOH{\cdot}H_2O$ in an oxygen gas atmosphere. The mixtures of starting regents in appropriate molar ratios were ground thoroughly, heated at 923 K for 12 h to drive off CO_2, and pressed into pellets. They were heated in oxygen flow at 1023 K for 72 h for the Fe solid solution and at 1073 K for 72 h for Co with intermittent grinding. Both the reacted materials were slowly cooled to room temperature over a period of 24 h to recover any oxygen lost during the high temperature reaction.

†Industrial Technology Fellow at NEDO.

 DOI: 10.1039/b200690c

ND data were collected on the powder diffractmeter, HERMES, at the institute of material research, Tohoku University, Japan Atomic Energy Research Institute (JAERI), Tokai.[14] The wavelength used, λ, was 1.82 Å. The data were collected at ambient temperature in the 2θ range 3–153° with a step width of 0.1°. Cylindrical vanadium cells of dimensions 10 mm in diameter and 50 mm in height were used. X-Ray diffraction (XRD) patterns were recorded with a Rigaku Rotaflex RU-200B/RINT using monochromatic Cu Kα radiation. The data were collected in the 2θ range 20–120° in a step scan mode with step width of 0.02°. The XRD and ND data were refined using the RIETAN 2000 program.[15] The neutron coherent scattering lengths, b_c ($\times 10^{-12}$ cm), were b_c(Li) = −0.190, b_c(Mn) = −0.373, b_c(Fe) = 0.945, b_c(Co) = 0.249, and b_c(O) = −0.5803.

X-Ray absorption measurements were carried out at beam line 10B of the Photon Factory at the National Laboratory for High Energy Physics (KEK-PF) (Proposal No. 2001G123). The measurements were performed in transmission mode at the Mn K-edge around 6.5 keV, Fe K-edge around 7.1 keV, and Co K-edge around 7.7 keV. The incident X-rays were monochromatized with a Si (311) crystal. The gases employed for the ionizing chambers to detect X-ray intensities were pure N_2 gas before the sample, and pure N_2 or an 85% N_2/15% Ar mixture after, depending upon the energy region. A grazing mirror was used for the suppression of higher harmonics in the Mn absorption measurements. Extended X-ray absorption fine structure (EXAFS) data were analyzed using Rigaku REX2000 software. The Fe K-edge absorption spectra were corrected by absorption of $LiMn_2O_4$ in the same energy range, because they are superposed on EXAFS data of Mn that appear above 6.6 keV. Backgrounds were subtracted by extrapolated a Victoreen-type function from the pre-edge region and EXAFS oscillations $\chi(k)$ were extracted using cubic spline base-line functions. Fourier transforms were performed on the normalized $\chi(k)$ with k^3 weighting of a Hanning window in the region of k = 2.3–10.5 Å^{-1} for Mn and Co and 2.3–8.5 Å^{-1} for Fe. Curve fitting was carried out using one shell models in the filtered range of R = 0.98–1.87 Å for Mn–O, 1.96–2.92 Å for Mn–M, 0.98–1.93 Å for Fe–O, 2.06–2.91 Å for Fe–M, 0.98–1.87 for Co–O, and 1.90–3.00 Å for Co–M. The coordinate number was fixed at 6. The back scattering factors and phase shifts were calculated using FEFF6,[16] assuming regular spinels, with the lattice parameter obtained by ND Rietveld refinement.

^{57}Fe Mössbauer measurements were carried out with an FGX-100 spectrometer (Topologic systems) at 300 K. α-Fe foil was used for velocity calibration. Collected data were fitted to a Lorentzian line shape using Mosswin ver. 2.0 software. Magnetization measurements were performed in a He atmosphere between 77 and 300 K using an MB-3 Shimadzu Faraday balance with Tutton's salt, $(NH_4)_2Mn(SO_4)_2{\cdot}6H_2O$, to calibrate the magnetization data.

For electrochemical charge and discharge, positive electrodes were made by coating a mixture of 87 wt% of the obtained samples, 5 wt% of acethylene black and 8 wt% of polyvinylidene fluoride onto an aluminium-foil current collector. The thickness of the positive electrodes was 40 μm. Coin-type cells were used for charge and discharge tests. Lithium foil of 0.2 mm thickness, 1 mol dm^{-3} $LiPF_6$ in propylene carbonate, and a glass fiber filter were employed as the negative electrode, electrolyte and separator, respectively. The rate of charge and discharge was 0.1 C (0.2–0.3 mA cm^{-2}, 0.015 mA mg^{-1}).

Results and discussion

Structure refinement

Fig. 1 shows XRD patterns of $LiFe_{0.5}Mn_{1.5}O_4$, $LiCo_{0.5}Mn_{1.5}O_4$ and $LiCoMnO_4$, which could be indexed with the cubic space group $Fd\bar{3}m$. A solid solution of $LiFe_xMn_{2-x}O_4$ formed for $0 \leqslant x \leqslant 0.5$ in our experimental conditions, whereas that of $LiCo_xMn_{2-x}O_4$ formed for $0 \leqslant x \leqslant 1.0$. In the x region above 0.5 of the Fe solid solution, another phase with a cubic structure like $LiFeO_2$ appeared and the spinel phase also seemed much broader (not shown). Minute impurity peaks appeared at 2θ = 44.8, 59.0 and 64.7° in $LiCoMnO_4$ as marked by the asterisks in Fig. 1. It could be considered that these arose from an inverse spinel phase (a = 8.11–8.15 Å) of Co_2MnO_4 (a = 8.269 Å) − Co_3O_4 (a = 8.0837 Å) intermediate components. In ND patterns of Fe and Co solid solutions, no superstructure reflection due to 1 : 3 order for x = 0.5 and 1 : 1 order for x = 1.0 was observed (Fig. 2), indicating that Fe (or Co) and Mn disorder over 16d sites. The appearance of an impurity peak at 2θ = 45.1° in $LiCoMnO_4$ could be assigned to the reflection (2 2 2), which gives the highest peak in the ND pattern of Co_2MnO_4. The minor impurity contains Co^{2+} and Mn^{3+} ions, suggesting the incomplete oxidation of these transition metal ions by our experimental conditions.

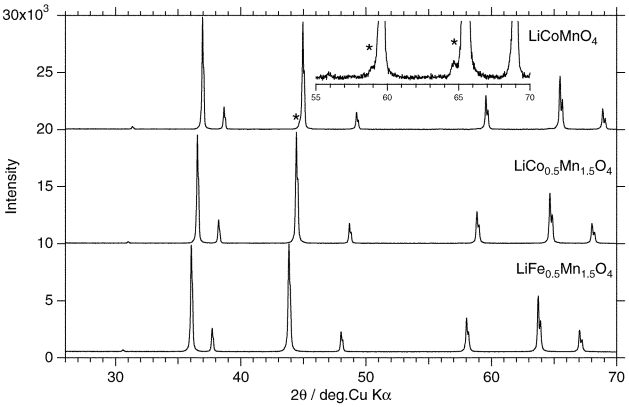

Fig. 1 XRD patterns of $LiFe_{0.5}Mn_{1.5}O_4$, $LiCo_{0.5}Mn_{1.5}O_4$, and $LiCoMnO_4$.

ND Rietveld analysis was carried out in order to obtain information about cation distribution. For Fe solid solutions, $LiFe_xMn_{2-x}O_4$ (x = 0, 0.1, 0.3, 0.5), structural refinement was adopted using three models which are: (1) $(Li)_{8a}[Fe_xMn_{2-x}]_{16d}O_4$, Li occupies tetrahedral 8a sites and Mn and Fe occupy octahedral 16d sites; (2) $(Li_{1-y}Fe_y)_{8a}[Fe_{x-y}Mn_{2-x}Li_y]_{16d}O_4$, Fe exists in both 8a and 16d sites; and (3) $(Li_{1-y}Mn_y)_{8a}[Fe_xMn_{2-x-y}Li_y]_{16d}O_4$. Mn exists in both 8a and 16d sites. The overall thermal parameters, B, were refined, since it is difficult to assign the B parameter for each site. The R_{wp} parameter and goodness of fit, S, were used to evaluate the refinement results. The R_{wp} and S parameters were smaller in model (2) with $y \leqslant 0.025$ than in model (1) when $x \geqslant 0.1$. In model (3), unexpectedly large y values were obtained. These indicate that Fe solid solutions have cation distributions of $(Li_{1-y}Fe_y)_{8a}[Fe_{x-y}Mn_{2-x}Li_y]_{16d}O_4$; the tetrahedral 8a site contains a small amount of Fe. Fig. 2(a) shows the observed, calculated, and the difference plots of $LiFe_{0.5}Mn_{1.5}O_4$. The structural parameters are given in Table 1(a), and the refined lattice parameters and cation distributions are summarized in Table 2. For the Co solid solution, $LiCo_xMn_{2-x}O_4$ (x = 0.5, 1.0), three similar models, where Co was replaced instead of Fe in the above models, were adopted. The R_{wp} and S parameters were smaller in model (2), with $y \leqslant 0.08$, than in model (1). Model (3) was not accepted because of a negative y value. These results indicate that $LiCo_xMn_{2-x}O_4$ (x = 0.5, 1.0) have a cation distribution of $(Li_{1-y}Co_y)_{8a}[Co_{x-y}Mn_{2-x}Li_y]_{16d}O_4$; some Co ions occupy tetrahedral 8a sites. Fig. 2(b) and (c) show the observed, calculated, and the difference plots of $LiCo_{0.5}Mn_{1.5}O_4$ and $LiCoMnO_4$, respectively. The structural parameters are given in Table 1(b) and (c), and the refined cation distributions are in Table 2. For Fe substitution, the

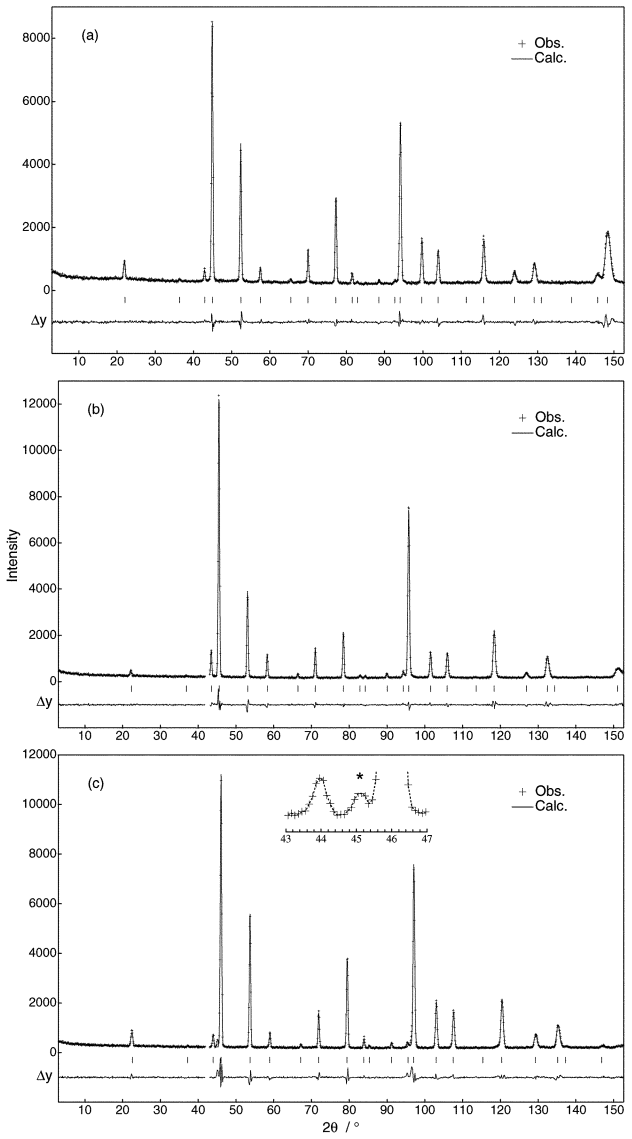

Fig. 2 Observed, calculated and difference plots of neutron diffraction for (a) $LiFe_{0.5}Mn_{1.5}O_4$, (b) $LiCo_{0.5}Mn_{1.5}O_4$, and (c) $LiCoMnO_4$. The solid line is calculated, dots indicate observed intensities and Δ_y is the difference between observed and calculated intensities.

lattice parameter *a* slightly increased and the amount of Fe disordered over the tetrahedral 8a sites increased with increasing *x*. For Co substitution, the lattice parameter *a* decreased and the amount of Co disordered to tetrahedral 8a sites increased with increasing *x*.

The powder neutron diffractometer used in this work has multi-detector system with an interval of 1° and 10 step-scan repetitions. Because the step of the obtained data is limited to 0.1°, that is 1500 points, the number of data points was much smaller than conventional XRD data that we collect with an interval of 0.02° for Rietveld refinement. Therefore the thermal parameter, *B*, could not be refined for each site due to the lower information quality of diffraction data. XRD Rietveld refinement results were added for comparison. Tables 3 and 4 give the structural parameters and final obtained lattice parameters and cation distributions obtained using model (2). The lattice parameters, *a*, and cation distributions were in good agreement with the ND Rietveld results, Table 2. The distribution of Fe over the 8a site and the 16d site was supported by ^{57}Fe Mössbauer spectroscopy at 300 K (Fig. 3). The spectrum, with a slightly asymmetric profile, could be fitted to two doublets with different isomer shift (IS) and quadrupole splitting (QS) values. Table 5 gives the fitting parameters for $LiFe_xMn_{2-x}O_4$ and other iron compounds. The IS value of the major component (I), +0.35 mm s^{-1}, could be attributed to high spin Fe^{3+} in octahedral 16d sites, since it is similar to those of octahedrally coordinated high spin Fe^{3+} in α-$LiFe_5O_8$ (+0.39 mm s^{-1}),[17] α-$LiFeO_2$ (+0.37 mm s^{-1}),[18] and α-$NaFeO_2$ (+0.37 mm s^{-1}),[19] Table 5. The minor component (II) with an IS value of +0.21–24 mm s^{-1} could be attributed to high spin Fe^{3+} in tetrahedral 8a sites because tetrahedrally coordinated high spin Fe^{3+} in α-$LiFe_5O_8$ shows a smaller IS value (+0.18 mm s^{-1}) than octahedrally coordinated Fe, Table 5. The ratios of Fe located in 8a sites to the substituted Fe were 4–5% for any *x* from the peak area ratios. These values were consistent with the cation distributions obtained from ND Rietveld analysis; the corresponding ratios were estimated as being 5.8 (±2.4), 9.0 (±4.7), and 15 (±18)% for $x = 0.5$, 0.3, and 0.1, respectively, Table 2.

Local structure of transition metals

Fig. 4(a) and (b) show Mn K-XANES spectra of $LiFe_xMn_{2-x}O_4$ ($x = 0$, 0.1, 0.3, 0.5) and $LiCo_xMn_{2-x}O_4$ ($x = 0$, 0.5, 1.0), respectively, with reference spectra of Mn_2O_3 and $LiMg_{0.5}Mn_{1.5}O_4$ where the valence states of Mn are 3+ and 4+, respectively. The spectrum of $LiMn_2O_4$ ($x = 0$), solid line, consists of a pre-edge absorption (A), two steps in the absorption edge (B_1 and B_2), and two resonances above the absorption edge (C and D). These features are characteristic of the octahedral 16d site in the spinel structure.[20] The overall spectral shape was very similar for substitution of Fe or Co, indicating six oxygen ions coordinated to Mn, which is similar to $LiMn_2O_4$. The absorption edges were shifted to higher energy with increasing Fe ($x \geqslant 0.3$) and Co substitutions, though it was very close to $LiMn_2O_4$ with $x = 0.1$ of Fe. This shift is correlated with an increase to over 3.5+ in the Mn oxidation state by Fe and Co substitution, as expected if Fe and Co ions replace trivalent Mn ions. $LiCoMnO_4$ was close to $LiMg_{0.5}Mn_{1.5}O_4$ in absorption edge energy, indicating Mn ions exist mainly in the 4+ state. The peak positions of resonances C and D were, however, unchanged by *x* in the Fe solid solution contrary to the overall shift in the Co solid solution. The XANES simulation reveals that the near edge structure is derived from multiple scattering to the third and fourth shells rather than the first two shells.[20] This means that the resonances C and D are affected by the average structure rather than the local structure around Mn. Therefore, it is considered that the peak positions of the resonances are unchanged in the Fe solid solutions because there is no significant change with *x* in the lattice parameter (Table 2). However, they are monotonously shifted with *x* in Co solid solutions according to the larger change in the lattice parameter (Table 2).

Fig. 5(a) shows Fe K-XANES spectra of $LiFe_xMn_{2-x}O_4$ ($x = 0.1$, 0.3, 0.5) with reference spectra of $ZnFe_2O_4$ and $FeSO_4 \cdot 7H_2O$ where Fe ions exist as 3+ and 2+ in valence, respectively, with octahedral coordination. The threshold energy was unchanged by Fe content, *x*, and close to that of trivalent references, $ZnFe_2O_4$. This indicates that Fe is 3+ in valence state in the solid solutions. Additionally, the overall profile was very similar to that of $ZnFe_2O_4$, a regular spinel – $(Zn^{2+})_{8a}[Fe^{3+}{}_2]_{16d}O_4$ (lattice parameter, $a = 8.47$ Å)[21] – suggesting that Fe ions are mainly located in octahedral 16d sites in the spinel structure. Fig. 5(b) shows Co K-XANES spectra of $LiCo_xMn_{2-x}O_4$ ($x = 0.5$, 1.0) with reference spectra of $LiCoO_2$ and $Co(acac)_2 \cdot 2H_2O$ [bis(2,4-pentadionato) Co(II) dihydrate] as 3+ and 2+, respectively, with octahedral coordination. The threshold energy was unchanged by Co content, *x*, and close to that of trivalent reference $LiCoO_2$, indicating that nearly all of the Co ions are 3+ in valence state in the solid solutions.

Fig. 6(a)–(d) illustrate the magnitude of the Fourier transformed EXAFS signal, F(*R*), of Mn K-edge and Fe K-edge in

Table 1 Neutron diffraction Rietveld refinement results for (a) $LiFe_{0.5}Mn_{1.5}O_4$, (b) $LiCo_{0.5}Mn_{1.5}O_4$, and (c) $LiCoMnO_4$

(a) $LiFe_{0.5}Mn_{1.5}O_4$[a]

Atom	Position	x	y	z	Occupancy	B/Å^2
Li(1)	8a	0.125	0.125	0.125	0.971(12)	0.78(18)
Fe(1)	8a	0.125	0.125	0.125	0.029(12)	= B[Li(1)]
Mn	16d	0.500	0.500	0.500	0.7500	= B[Li(1)]
Fe(2)	16d	0.500	0.500	0.500	0.2356(6)	= B[Li(1)]
Li(2)	16d	0.500	0.500	0.500	0.0144(6)	= B[Li(1)]
O	32e	0.2629(3)	0.2629(3)	0.2629(3)	1.0000	= B[Li(1)]

(b) $LiCo_{0.5}Mn_{1.5}O_4$[b]

Atom	Position	x	y	z	Occupancy	B/Å^2
Li(1)	8a	0.125	0.125	0.125	0.98(2)	0.90(15)
Co(1)	8a	0.125	0.125	0.125	0.02(2)	= B[Li(1)]
Mn	16d	0.500	0.500	0.500	0.7500	= B[Li(1)]
Co(2)	16d	0.500	0.500	0.500	0.24(4)	= B[Li(1)]
Li(2)	16d	0.500	0.500	0.500	0.01(4)	= B[Li(1)]
O	32e	0.2633(3)	0.2633(3)	0.2633(3)	1.0000	= B[Li(1)]

(c) $LiCoMnO_4$[c]

Atom	Position	x	y	z	Occupancy	B/Å^2
Li(1)	8a	0.125	0.125	0.125	0.93(4)	0.5(3)
Co(1)	8a	0.125	0.125	0.125	0.07(4)	= B[Li(1)]
Mn	16d	0.500	0.500	0.500	0.5000	= B[Li(1)]
Co(2)	16d	0.500	0.500	0.500	0.47(8)	= B[Li(1)]
Li(2)	16d	0.500	0.500	0.500	0.03(8)	= B[Li(1)]
O	32e	0.2629(5)	0.2629(5)	0.2629(5)	1.0000	= B[Li(1)]

[a]Space group $Fd\bar{3}m$, a = 8.2447(3) Å, R_{wp} = 6.92, R_p = 5.33, $S = R_{wp}/R_e$ = 1.41, R_I = 3.08, R_F = 2.97. [b]Space group $Fd\bar{3}m$, a = 8.1387(3) Å, R_{wp} = 7.13, R_p = 5.47, $S = R_{wp}/R_e$ = 1.31, R_I = 3.29, R_F = 2.71. [c]Space group $Fd\bar{3}m$, a = 8.0565(4) Å, R_{wp} = 9.52, R_p = 6.58, $S = R_{wp}/R_e$ = 1.83, R_I = 4.62, R_F = 3.23.

$LiFe_{0.5}Mn_{1.5}O_4$, and Mn K-edge and Co K-edge in $LiCoMnO_4$, respectively. Phase correction has not been applied to the F(R) presented, so the peaks are shifted by approximately −0.4 Å from the actual bond distances. The first peaks at 1.5 Å correspond to Mn–O, Fe–O, or Co–O pairs in the first coordination sphere. The second peaks at around 2.5 Å correspond to the Mn–M, Fe–M, (M = Mn and Fe), or Co–M (M = Mn and Co) interaction in the second coordination sphere. They include a small contribution from M–Li interaction, which could be negligible because of the small back scattering amplitude of the Li atom. Curve fitting results to the filtered EXAFS signal of the first and second neighbor peaks of F(R) are shown in the insets of Fig. 6. Table 6 gives obtained interatomic distances and Debye–Waller factors. For x = 0.1 and 0.3 in $LiFe_xMn_{2-x}O_4$, we could not obtain a satisfactory Fe-EXAFS signal with enough S : N for analysis because of overlap with the large absorption of Mn. Fig. 7(a) and (b) show the compositional dependence of calculated M–O and M–M interatomic distances, respectively, in Fe and Co solid solutions. The Mn–O and Mn–M distances (■) did not vary with x in $LiFe_xMn_{2-x}O_4$ whereas they largely decreased with increasing x in $LiCo_xMn_{2-x}O_4$ (▲). These variations in interatomic distances were associated with the lattice parameter. The average interatomic distances, M_{16d}–O_{32e} and M_{16d}–M_{16d}, which were calculated from the lattice parameters obtained by ND Rietveld analysis, are plotted together in Fig. 7 as open squares (□) and upward triangles (△), respectively. This represents that the changes in Mn–O and Mn–M distances are comparable to those in calculated M_{16d}–O_{32e} and M_{16d}–M_{16d}.

The interatomic distances from the central Fe and Co atoms, Fe(Co)–O and Fe(Co)–M, were different from Mn–O and Mn–M in the compounds (Table 6, ● and ▼ in Fig. 7). The Co–O distance was shorter than Mn–O distance, suggesting the local contraction around Co. It is considered that this contraction around Co occurs because of the smaller ionic radius of Co^{3+} [0.545 Å as low spin (LS) in octahedral coordination – the description of the spin state is in the following section][22] than Mn^{3+} [0.645 Å as high spin (HS) in octahedral coordination].[22] Though the Co–M distance was also shorter than Mn–M in $LiCo_{0.5}Mn_{1.5}O_4$, they became closer in $LiCoMnO_4$. This implies that Co and Mn homogeneously distribute in the octahedrally coordinated 16d sites. On the other hand, the Fe–O distance was longer than the Mn–O distance, indicating the local expansion around Fe. The Fe–M distance was also longer than Mn–M. Fe^{3+} (0.645 Å for HS in the octahedral coordination)[22] is equal to Mn^{3+} in ionic radius but it is a non-Jahn–Teller ion. It is supposed that the lattice strain is induced by substituting Fe^{3+} of the non-Jahn–Teller ion, since clustering of Jahn–Teller Mn^{3+} ions make

Table 2 Lattice parameters, a, cation distributions, and isotropic atomic displacement parameters, B, of $LiFe_xMn_{2-x}O_4$ (x = 0, 0.1, 0.3, 0.5) and $LiCo_xMn_{2-x}O_4$ (x = 0.5, 1.0) refined by neutron diffraction Rietveld analysis

Sample	a/Å	Cation distribution	B/Å^2
$LiMn_2O_4$	8.2312(4)	$(Li_{1.000})_{8a}[Mn_{2.000}]_{16d}O_4$	0.95(18)
$LiFe_{0.1}Mn_{1.9}O_4$	8.2354(4)	$(Li_{0.985}Fe_{0.015(18)})_{8a}[Mn_{1.9}Fe_{0.085}Li_{0.015}]_{16d}O_4$	0.93(17)
$LiFe_{0.3}Mn_{1.7}O_4$	8.2391(4)	$(Li_{0.973}Fe_{0.027(14)})_{8a}[Mn_{1.7}Fe_{0.273}Li_{0.027}]_{16d}O_4$	0.82(18)
$LiFe_{0.5}Mn_{1.5}O_4$	8.2447(3)	$(Li_{0.971}Fe_{0.029(12)})_{8a}[Mn_{1.5}Fe_{0.471}Li_{0.029}]_{16d}O_4$	0.78(18)
$LiCo_{0.5}Mn_{1.5}O_4$	8.1387(3)	$(Li_{0.98}Co_{0.02(2)})_{8a}[Mn_{1.5}Co_{0.48}Li_{0.02}]_{16d}O_4$	0.90(15)
$LiCo_{1.0}Mn_{1.0}O_4$	8.0565(4)	$(Li_{0.93}Co_{0.07(4)})_{8a}[Mn_{1.0}Co_{0.93}Li_{0.07}]_{16d}O_4$	0.5(3)

Table 3 X-ray diffraction Rietveld refinement results for (a) $LiFe_{0.5}Mn_{1.5}O_4$, (b) $LiCo_{0.5}Mn_{1.5}O_4$, and (c) $LiCoMnO_4$

(a) $LiFe_{0.5}Mn_{1.5}O_4$[a]

Atom	Position	x	y	z	Occupancy	B/Å^2
Li(1)	8a	0.125	0.125	0.125	0.968(3)	1.8(2)
Fe(1)	8a	0.125	0.125	0.125	0.032(3)	= B[Li(1)]
Mn	16d	0.500	0.500	0.500	0.7500	0.664(16)
Fe(2)	16d	0.500	0.500	0.500	0.234(6)	= B(Mn)
Li(2)	16d	0.500	0.500	0.500	0.016(6)	= B(Mn)
O	32e	0.26270(15)	0.26270(15)	0.26270(15)	1.0000	1.06(4)

(b) $LiCo_{0.5}Mn_{1.5}O_4$[b]

Atom	Position	x	y	z	Occupancy	B/Å^2
Li(1)	8a	0.125	0.125	0.125	0.985(3)	1.7(3)
Co(1)	8a	0.125	0.125	0.125	0.015(3)	= B[Li(1)]
Mn	16d	0.500	0.500	0.500	0.7500	0.549(15)
Co(2)	16d	0.500	0.500	0.500	0.242(6)	= B(Mn)
Li(2)	16d	0.500	0.500	0.500	0.008(6)	= B(Mn)
O	32e	0.26268(15)	0.26268(15)	0.26268(15)	1.0000	0.89(4)

(c) $LiCoMnO_4$[c]

Atom	Position	x	y	z	Occupancy	B/Å^2
Li(1)	8a	0.125	0.125	0.125	0.925(4)	2.6(3)
Co(1)	8a	0.125	0.125	0.125	0.075(4)	= B[Li(1)]
Mn	16d	0.500	0.500	0.500	0.5000	0.53(2)
Co(2)	16d	0.500	0.500	0.500	0.462(8)	= B(Mn)
Li(2)	16d	0.500	0.500	0.500	0.038(8)	= B(Mn)
O	32e	0.2632(2)	0.2632(2)	0.2632(2)	1.0000	0.78(5)

[a]Space group $Fd\bar{3}m$, a = 8.24778(3) Å, R_{wp} = 11.82, R_p = 8.54, $S = R_{wp}/R_e$ = 1.37, R_I = 1.95, R_F = 1.53. [b]Space group $Fd\bar{3}m$, a = 8.14148(3) Å, R_{wp} = 11.27, R_p = 7.82, $S = R_{wp}/R_e$ = 1.29, R_I = 1.60, R_F = 1.19. [c]Space group $Fd\bar{3}m$, a = 8.05331(3) Å, R_{wp} = 15.58, R_p = 11.34, $S = R_{wp}/R_e$ = 1.74, R_I = 3.06, R_F = 2.36.

Table 4 Lattice parameters, a, and cation distributions of $LiFe_xMn_{2-x}O_4$ (x = 0, 0.1, 0.3, 0.5) and $LiCo_xMn_{2-x}O_4$ (x = 0.5, 1.0) refined by XRD Rietveld analysis

Sample	a/Å	Cation distribution
$LiMn_2O_4$	8.23436(7)	$(Li_{1.0000})_{8a}[Mn_{2.0000}]_{16d}O_4$
$LiFe_{0.1}Mn_{1.9}O_4$	8.23938(5)	$(Li_{0.984}Fe_{0.016(3)})_{8a}[Mn_{1.9}Fe_{0.084}Li_{0.016}]_{16d}O_4$
$LiFe_{0.3}Mn_{1.7}O_4$	8.24403(4)	$(Li_{0.973}Fe_{0.027(3)})_{8a}[Mn_{1.7}Fe_{0.273}Li_{0.027}]_{16d}O_4$
$LiFe_{0.5}Mn_{1.5}O_4$	8.24778(3)	$(Li_{0.968}Fe_{0.032(3)})_{8a}[Mn_{1.5}Fe_{0.468}Li_{0.032}]_{16d}O_4$
$LiCo_{0.5}Mn_{1.5}O_4$	8.14148(3)	$(Li_{0.985}Co_{0.015(3)})_{8a}[Mn_{1.5}Co_{0.485}Li_{0.015}]_{16d}O_4$
$LiCo_{1.0}Mn_{1.0}O_4$	8.05331(3)	$(Li_{0.925}Co_{0.075(4)})_{8a}[Mn_{1.0}Co_{0.925}Li_{0.075}]_{16d}O_4$

volume loss. It is considered, on the contrary, that the lattice strain is reduced by smaller non-Jahn–Teller Co^{3+} in the Co solid solution.

Magnetic measurements

Fig. 8(a) shows the field dependence of magnetization observed at 77 and 300 K for $LiFe_{0.5}Mn_{1.5}O_4$ and $LiCoMnO_4$. A small spontaneous magnetization was observed in $LiFe_{0.5}Mn_{1.5}O_4$ (σ_s = 0.035 Gcm^3 g^{-1} at 300 K), indicating the inclusion of ferromagnetic or ferrimagnetic impurities. The impurity content was estimated to be 0.05 wt%, assuming it to be $LiFe_5O_8$ (σ_s = 65 Gcm^3 g^{-1} at 300 K) which usually appears in the synthesis of Li–Fe oxide. On the other hand, no spontaneous magnetization was observed above 77 K in Co solid solutions, in spite of the existence of impurity phases of Co_2MnO_4 and Co_3O_4 intermediate components indicated by XRD and ND measurements. It was considered that these could not be detected due to the lower transition temperature of Co_3O_4 (Tc = 33 K)[23] and/or the smaller spontaneous magnetization value of Co_2MnO_4 (σ_s = 12 Gcm^3 g^{-1} at 80 K, Tc = 170–180 K).[24]

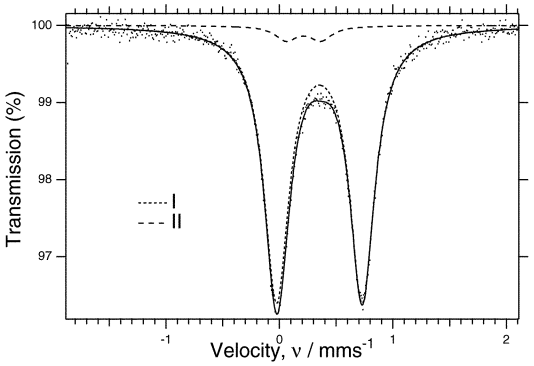

Fig. 3 ^{57}Fe Mössbauer spectra of $LiFe_{0.5}Mn_{1.5}O_4$ at 300 K. Dots and solid lines are observed and calculated spectra, respectively. Short and long dashed lines correspond to the calculated doublets which are components I and II, respectively, in Table 5.

Since spontaneous magnetization was much less in any samples consequently, the inverse molar magnetization normalized by magnetic field, H/M could be considered as the inverse molar susceptibility, χ_m^{-1}. The temperature dependence of χ_m^{-1} is shown in Fig. 8(b). Curie–Weiss paramagnetic behavior was observed above 150 K for all samples, and therefore, the effective paramagnetic moment, μ_{eff}, and Weiss temperature, θ, values were calculated from these plots (Table 7). The Weiss temperature for every sample was a smaller negative value compared to that of $LiMn_2O_4$.[25] This change could be explained by the increase of the ferromagnetic 90° Mn^{4+}–O interaction. The experimental values of

Table 5 ^{57}Fe Mössbauer parameters for $LiFe_xMn_{2-x}O_4$ samples and various iron oxides at 300 K

Sample	Component	IS/mm s^{-1}	QS/mm s^{-1}	Γ/mm s^{-1}	Area (%)
$LiFe_{0.1}Mn_{1.9}O_4$	I	+0.3548(8)	0.7673(14)	0.254(3)	94.8
	II	+0.23(2)	0.25(5)	0.36(15)	5.2
$LiFe_{0.3}Mn_{1.7}O_4$	I	+0.3526(7)	0.7607(15)	0.255(3)	95.6
	II	+0.243(13)	0.30(2)	0.21(4)	4.4
$LiFe_{0.5}Mn_{1.5}O_4$	I	+0.3519(7)	0.7554(13)	0.266(2)	95.6
	II	+0.211(13)	0.31(2)	0.24(4)	4.4
α-$LiFe_5O_8$ (ref. 17)	Fe^{3+} (HS)	+0.39			
	Fe^{3+} (HS)	+0.18			
α-$LiFeO_2$ (ref. 18)	Fe^{3+} (HS)	+0.37			
α-$NaFeO_2$ (ref. 19)	Fe^{3+} (HS)	+0.37			

μ_{eff} were close to the expected ones (Table 7) calculated by assuming $[Li_{1.0}]_{8a}[(Mn^{4+})_{1.0}(Mn^{3+}(HS))_{0.5}(Fe^{3+}(HS))_{0.5}]_{16d}O_4$ and $[Li_{1.0}]_{8a}[(Mn^{4+})_{1.0}(Mn^{3+}(HS))_{1.0-x}(Co^{3+}(LS))_x]_{16d}O_4$ ($x = 0.5$, 1.0), using the spin only paramagnetic moments, $2\sqrt{S(S+1)}$, where S is the quantum number, for Mn^{3+}(HS) ($S = 2$), Mn^{4+} ($S = 3/2$), Fe^{3+}(HS) ($S = 5/2$), and Co^{3+}(LS) ($S = 0$). This indicates that the substituted cations of Fe and Co on the 16d sites are in the high and low spin trivalent states, respectively.

Electrochemical property

Fig. 9 shows charge/discharge curves of the 2nd, 10th and 25th cycles between 3.0 and 5.3 V of $Li/LiFe_yMn_{2-y}O_4$ ($y = 0.1$, 0.3, 0.5) cells. The electrolyte oxidation on carbon black and active materials occurred in the higher voltage range around 5 V, especially at the first charge, so that the second cycle curve is shown instead of the first cycle. There appeared two reversible plateaus centered at 4.0 and 5.0 V. The capacities increased at the 5 V region and decreased at the 4 V region with increasing Fe content, y. Table 8 gives the observed capacities at the 2nd discharge and the theoretical capacities. The origin of the 5 V plateau that occurs during delithiation of $LiM_xMn_{2-x}O_4$ (M = transition metal) has been debated. *In-situ* XAFS studies in electrochemically delithiated $LiM_xMn_{2-x}O_4$ (M = Cr, Co, and Ni) have indicated that the 5 V capacity is associated with the removal of an electron from the M 3d orbital[11–13] and/or the oxygen 2p orbital.[26] For M = Fe, the changes in *in-situ*^{57}Fe Mössbauer spectra during delithiation exhibited the oxidation of Fe^{3+} to Fe^{4+} in part of Fe at the 5 V plateau, although the whole of Fe should be oxidized to the tetravalent state for its charge compensation.[8,27] Therefore, it has been supposed that the formation of holes over Fe 3d and O 2p bands contributes to the 5 V capacity. Here, however, the 5 and 4 V theoretical capacities are presumed to be the capacities obtained by the whole oxidation reactions of $Fe^{3+}{}_{16d} \rightarrow Fe^{4+}{}_{16d}$ and $Mn^{3+}{}_{16d} \rightarrow Mn^{4+}{}_{16d}$, respectively, for convenience, and the total theoretical capacity to the sum of them. The amounts of Fe and Mn ions in 16d sites were estimated from the distribution formula refined by ND Rietveld analysis, Table 2, and the substitution of Fe^{3+} for Mn^{3+} in this solid solution was indicated by the above XANES and magnetic studies. The ratio of the observed 2nd discharge capacity to the theoretical capacity, $C_{2nd}/C_{theo.}$, was *ca.* 0.9 at the total capacity for each Fe content, y. $C_{2nd}/C_{theo.}$ was less at the 5 V region than at the 4 V region. The Coulombic efficiency, C_d/C_c, at the 5 V plateau was *ca.* 0.6 for every value of y, while it was 1.0 at the 4 V region.

The cell cyclabilities are shown in the insets of Fig. 9. The

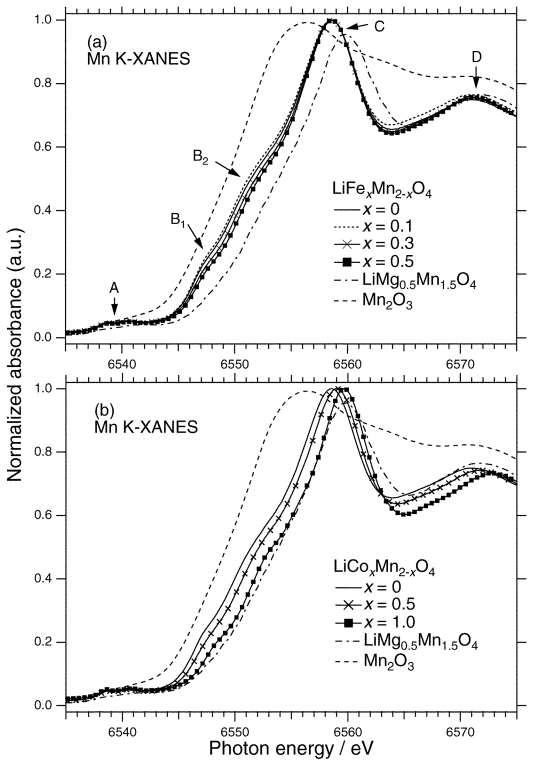

Fig. 4 Mn K-XANES spectra of (a) $LiFe_xMn_{2-x}O_4$ ($x = 0$, 0.1, 0.3, 0.5) and (b) $LiCo_xMn_{2-x}O_4$ ($x = 0$, 0.5, 1.0) with reference spectra of $LiMg_{0.5}Mn_{1.5}O_4$ and Mn_2O_3.

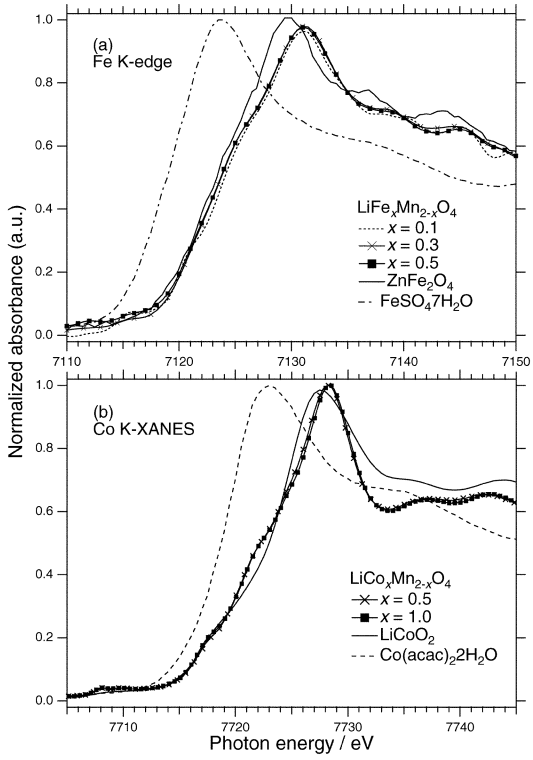

Fig. 5 (a) Fe K-XANES spectra of $LiFe_xMn_{2-x}O_4$ ($x = 0.1$, 0.3, 0.5) with reference spectra of $ZnFe_2O_4$ and $FeSO_4{\cdot}7H_2O$. (b) Co K-XANES spectra of $LiCo_xMn_{2-x}O_4$ ($x = 0.5$, 1.0) with reference spectra of $LiCoO_2$ and $Co(acac)_2{\cdot}2H_2O$.

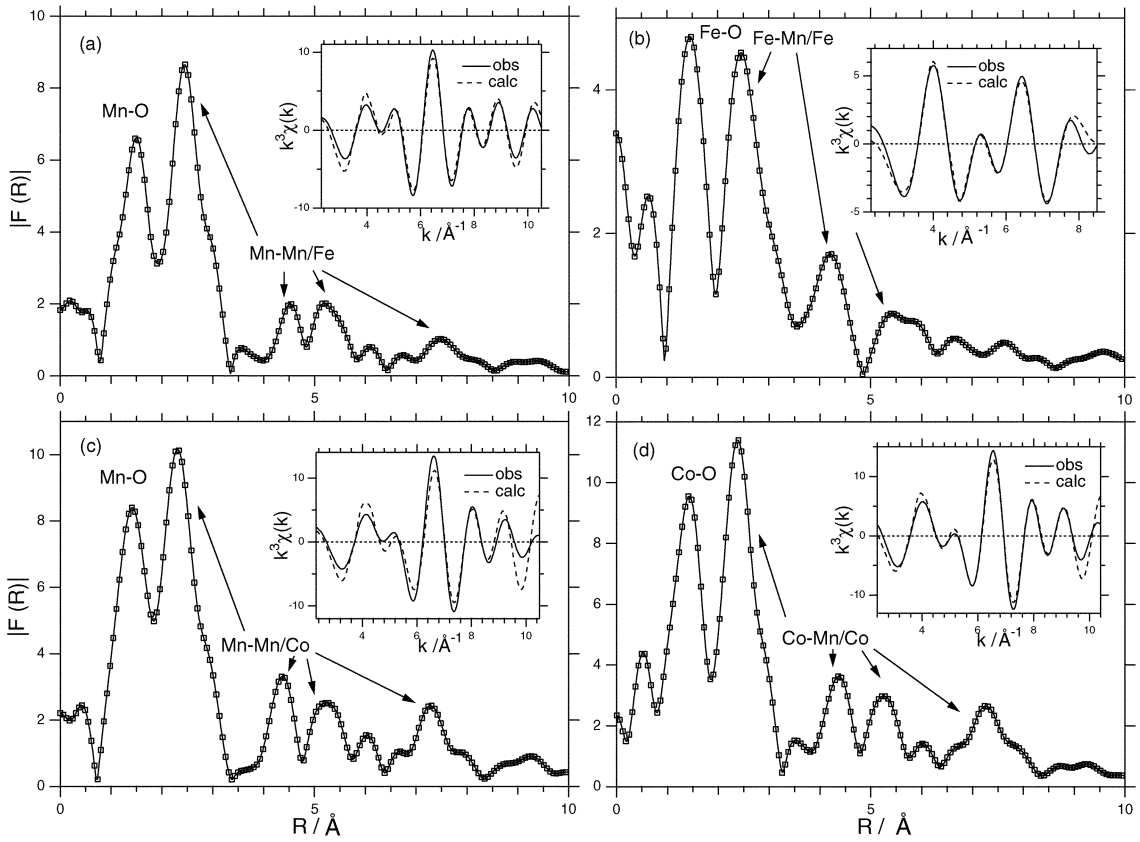

Fig. 6 Magnitude of Fourier transformed EXAFS signal, F(R): (a) Mn K-edge and (b) Fe K-edge in $LiFe_{0.5}Mn_{1.5}O_4$, and (c) Mn K-edge and (d) Co K-edge in $LiCoMnO_4$. The insets are the corresponding curve fitting results to the filtered EXAFS signal of the first and second neighbor of F(R). Solid and broken lines correspond to the observed and calculated signals, respectively.

Table 6 Interatomic distances and Debye–Waller factors in $LiFe_xMn_{2-x}O_4$ (x = 0, 0.1, 0.3, 0.5) and $LiCo_xMn_{2-x}O_4$ (x = 0.5, 1.0) obtained by EXAFS analysis

	Mn–O		Mn–M		Co(Fe)–O		Co(Fe)–M	
Sample	R/Å	σ/Å	R/Å	σ/Å	R/Å	σ/Å	R/Å	σ/Å
$LiMn_2O_4$	1.95	0.07	2.91	0.08				
$LiFe_{0.1}Mn_{1.9}O_4$	1.95	0.07	2.92	0.08				
$LiFe_{0.3}Mn_{1.7}O_4$	1.95	0.07	2.92	0.08				
$LiFe_{0.5}Mn_{1.5}O_4$	1.95	0.07	2.92	0.08	1.99	0.09	2.94	0.14
$LiCo_{0.5}Mn_{1.5}O_4$	1.94	0.07	2.88	0.07	1.91	0.06	2.86	0.08
$LiCo_{1.0}Mn_{1.0}O_4$	1.92	0.07	2.85	0.07	1.91	0.07	2.84	0.09

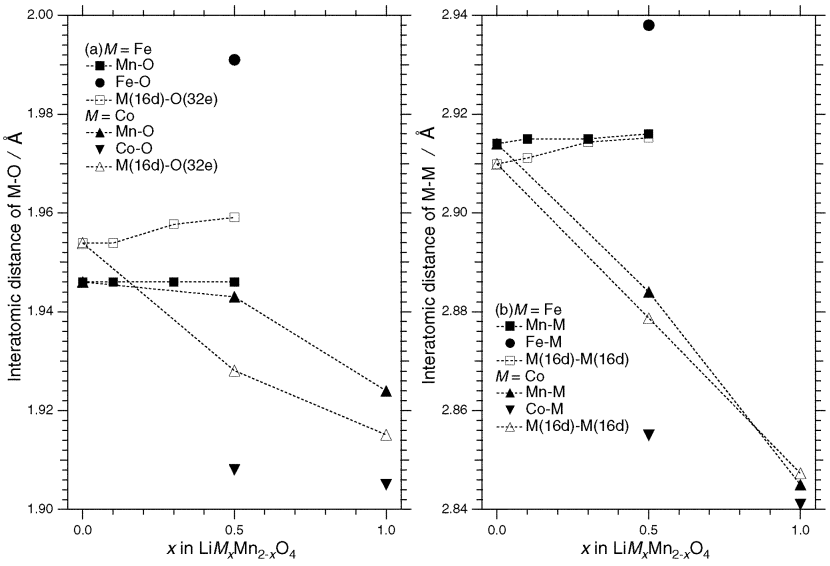

Fig. 7 Compositional dependence of interatomic distances: (a) Mn–O and Fe–O in $LiFe_xMn_{2-x}O_4$, and Mn–O and Co–O in $LiCo_xMn_{2-x}O_4$; (b) Mn–M and Fe–M in $LiFe_xMn_{2-x}O_4$ (M = Mn and Fe), and Mn–M and Co–M in $LiCo_xMn_{2-x}O_4$ (M = Mn and Co), obtained by the curve fitting analysis of EXAFS regions. The average M_{16d}–O_{32e} and M_{16d}–M_{16d} were calculated from the lattice parameters.

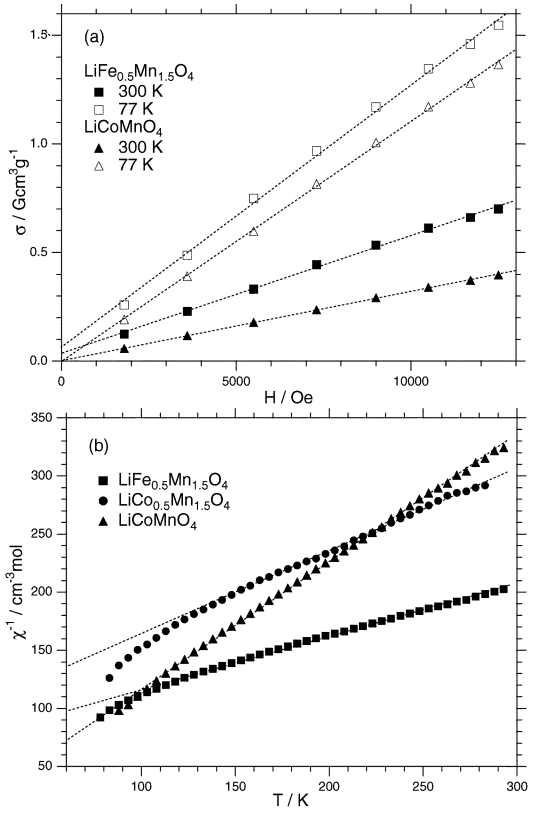

Fig. 8 (a) Field dependence of the magnetization, σ, at 300 and 77 K for $LiFe_{0.5}Mn_{1.5}O_4$ and $LiCoMnO_4$. (b) Temperature dependence of inverse molar susceptibility, χ_m^{-1}, for $LiFe_{0.5}Mn_{1.5}O_4$, $LiCo_{0.5}Mn_{1.5}O_4$, and $LiCoMnO_4$.

discharge capacities at the 2nd and 20th cycles and the ratio of them are given in Table 8. The variation in total discharge ratio, C_{d20th}/C_{d2nd}, indicates that the capacity fading became significant with increasing Fe content, y. The ratio, C_{20th}/C_{2nd}, was smaller at the 5 V-region in $y = 0.3$, and especially 0.5, than at the 4 V region. This implies that the capacity fading is governed by the irreversibility at the 5 V region in these y values. In $y = 0.1$, the 4 V region seemed dominant for capacity fading rather than at 5 V because C_{20th}/C_{2nd} values were 1.0 and 0.9 in 5 V and 4 V regions, respectively. Plateaus at 3.3 and 4.5 V can be seen in $y = 0.1$ [marked with arrows in Fig. 9 (a)]. Oxygen deficiency in samples is considered to account for these plateaus and is thought to be one of the causes of capacity fading at the 4 V region.[28] Therefore the oxygen deficiency might be a reason for the capacity fading in the $y = 0.1$ sample. It is considered, however, that the oxygen deficiency is much less in the sample because no endothermic and exothermic peak pair appeared around 280 K at differential scanning calorimetry (DSC) measurement (not shown), which is assigned to a phase transition from cubic to tetragonal and is regarded as a typical phenomenon for oxygen-deficient spinels.[29]

Fig. 10 and the insets show charge/discharge curves of the 2nd, 10th, and 22nd (for $y = 0.5$) or 25th ($y = 1.0$) cycles and the cyclabilities between 3.0 and 5.3 V of $Li/LiCo_yMn_{2-y}O_4$ cells. The 5 and 4 V theoretical capacities given in Table 8 were presumed to be the oxidation reactions of $Co^{3+}{}_{16d} \rightarrow Co^{4+}{}_{16d}$

Table 7 Magnetic parameters for $LiFe_{0.5}Mn_{1.5}O_4$ and $LiCo_xMn_{2-x}O_4$ ($x = 0.5$, 1.0)

Sample	μ_{eff}/μ_B (obs.)	μ_{eff}/μ_B (calc.)	θ/K
$LiMn_2O_4$ (ref. 25)	4.36	4.36	−266
$LiFe_{0.5}Mn_{1.5}O_4$	4.19	4.72	−177
$LiCo_{0.5}Mn_{1.5}O_4$	3.34	3.67	−129
$LiCo_{1.0}Mn_{1.0}O_4$	2.70	2.74	−6

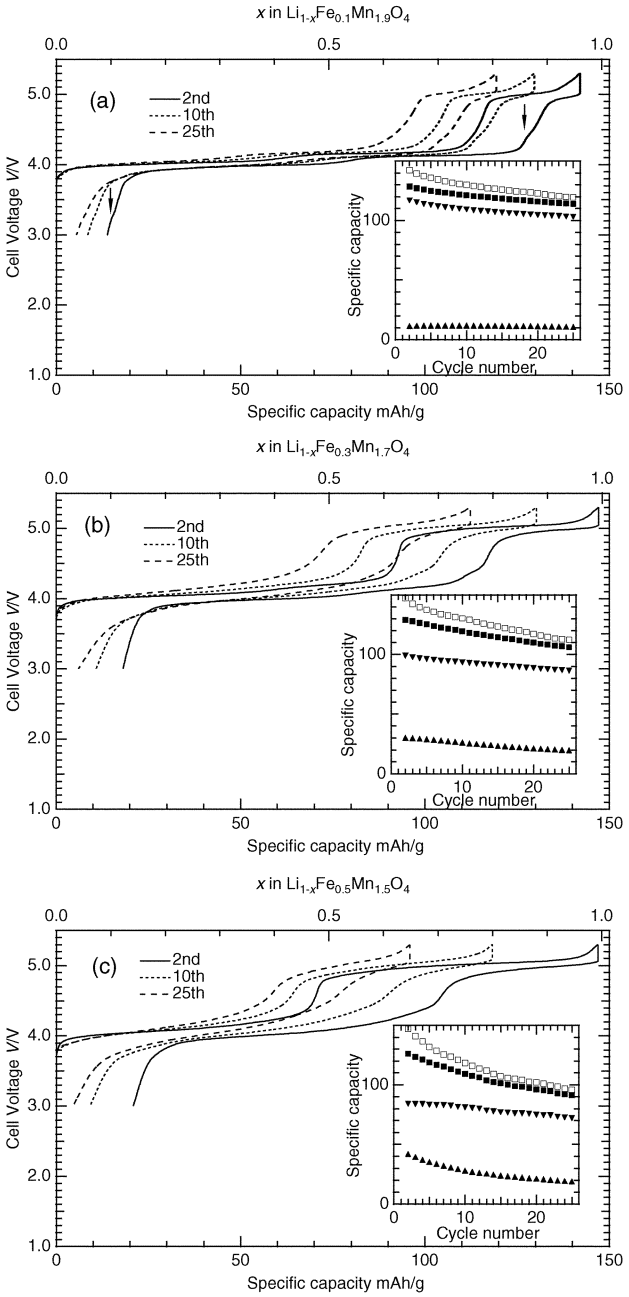

Fig. 9 Voltage–capacity profiles of the 2nd, 10th, and 25th cycles in $LiFe_xMn_{2-x}O_4$ [$x = 0.1$(a), 0.3 (b), 0.5 (c)]; electrolyte: 1.0 mol dm^{-3} $LiPF_6$/propylene carbonate; counter electrode: Li foil; charge and discharge rate: 0.1 C; charge and discharge cut-off voltage: 5.3 and 3.0 V. The insets plot the variation in the capacities upon cycling; total charge: □; total discharge: ■; 5 V discharge: ▲; 4 V discharge: ▼. The total, 5 and 4 V capacities correspond to the capacities of 5.3–3.0 V, 5.3–4.6 V and 4.6–3.0 V, respectively.

and $Mn^{3+}{}_{16d} \rightarrow Mn^{4+}{}_{16d}$, respectively, similar to Fe solid solutions. The amounts of Co and Mn ions in 16d sites were estimated from the distribution formula refined by ND Rietveld analysis, Table 2, and the substitution of Co^{3+} for Mn^{3+} in this solid solution was indicated by the above XANES and magnetic studies. Two plateaus centered at 3.9 and 5.1 V appeared on charge and discharge curves. In $y = 1.0$, a capacity of 3.9 V appeared, indicating that a small amount of Mn ions exists as 3+ due to imperfect incorporation of Co into the $LiMn_2O_4$ spinel, though it is expected as $Li^+Co^{3+}Mn^{4+}O_4$. The cyclability was better in Co-substituted samples compared with Fe samples. The ratios C_{d20th}/C_{d2nd} in both the total and 5 V capacities were more for $y = 0.5$ and even $y = 1.0$ of Co substitution than for $y = 0.5$ of Fe substitution. To find the

Table 8 Observed and theoretical capacity in $LiFe_xMn_{2-x}O_4$ ($x = 0.1, 0.3, 0.5$) and $LiCo_xMn_{2-x}O_4$ ($x = 0.5, 1.0$). The 5 and 4 V capacities correspond to 5.3–4.6 V and 4.6–3.0 V, respectively for Fe solid solutions, and correspond to 5.3–4.4 V and 4.4–3.0 V for Co solid solutions

	Total capacity			5 V capacity			4 V capacity		
Sample	C_{2nd}	$C_{theo.}$	$C_{2nd}/C_{theo.}$	C_{2nd}	$C_{theo.}$	$C_{2nd}/C_{theo.}$	C_{2nd}	$C_{theo.}$	$C_{2nd}/C_{theo.}$
$LiFe_{0.1}Mn_{1.9}O_4$	128	146	0.88	11	13	0.85	117	133	0.88
$LiFe_{0.3}Mn_{1.7}O_4$	129	144	0.90	30	40	0.75	99	104	0.95
$LiFe_{0.5}Mn_{1.5}O_4$	126	144	0.88	42	70	0.60	84	74	0.88
$LiCo_{0.5}Mn_{1.5}O_4$	121	143	0.85	51	70	0.73	70	73	0.96
$LiCo_{1.0}Mn_{1.0}O_4$	104	135	0.77	93	135	0.69	11	0	—
	C_{2nd}	C_{20th}	C_{2nd}/C_{20th}	C_{2nd}	C_{20th}	C_{2nd}/C_{20th}	C_{2nd}	C_{20th}	C_{2nd}/C_{20th}
$LiFe_{0.1}Mn_{1.9}O_4$	128	116	0.91	11	11	1.00	117	105	0.90
$LiFe_{0.3}Mn_{1.7}O_4$	129	110	0.85	30	21	0.70	99	89	0.90
$LiFe_{0.5}Mn_{1.5}O_4$	126	96	0.76	42	21	0.50	84	75	0.89
$LiCo_{0.5}Mn_{1.5}O_4$	121	106	0.88	51	45	0.88	70	61	0.87
$LiCo_{1.0}Mn_{1.0}O_4$	104	87	0.84	93	76	0.82	11	11	1.00

cause of such cyclic fading requires investigations of structural change during and/or after cycles. Indeed, it is difficult to remove the oxidation of liquid electrolytes at the 5 V region from the electrode performance of the material itself. For Cr substitution, $LiCr_xMn_{2-x}O_4$ ($0 \leqslant x \leqslant 1.0$), it was reported that the irreversible migration of some transition metals from the 16d site to 8a or to the 16c site occurred during charge up to 5.1 V and accounted for the experimental capacity loss especially at the 5 V region.[30] Such a migration, however, is not observed at least at the first cycle of $LiFe_{0.5}Mn_{1.5}O_4$.[8] Although further studies were needed to clarify the reason for cyclic fading, it could be mentioned that the transition metals initially disordered to the 8a site have little effect. $LiCoMnO_4$ showed better cyclability than $LiFe_{0.5}Mn_{1.5}O_4$ in spite of *ca.* 8% Co occupation at the 8a site, found by ND Rietveld refinement, Table 2. Additionally, it is considered to be important to investigate the change in the local structures around electrochemicallt active ions by Li-extraction/reinsertion, since their environments are distinct from each other, as revealed above by XAFS analysis.

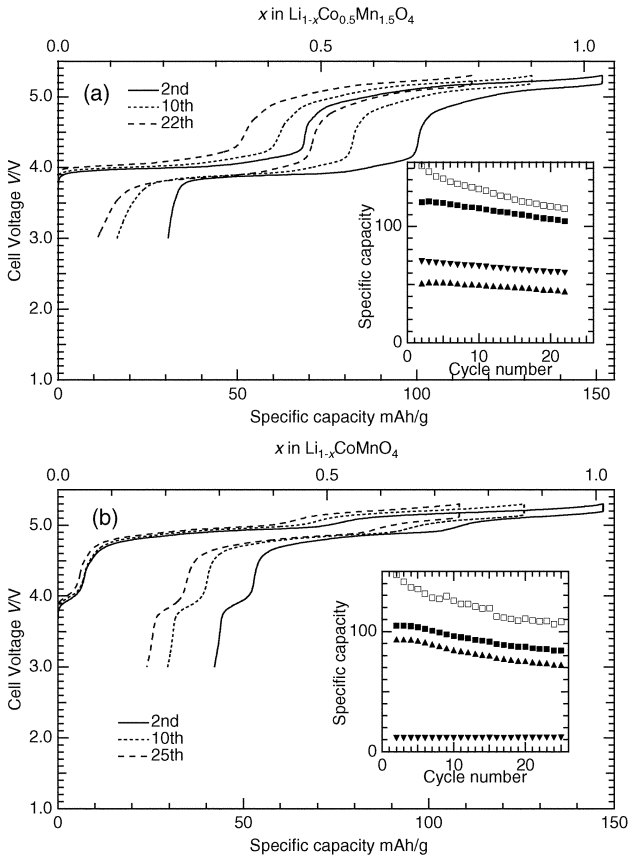

Fig. 10 Voltage–capacity profiles of the 2nd, 10th, and 25th (22nd) cycles in $LiCo_xMn_{2-x}O_4$ [$x = 0.5$ (a), 1.0 (b)]; electrolyte: 1.0 mol dm^{-3} $LiPF_6$/propylene carbonate; counter electrode: Li foil; charge and discharge rate: 0.1 C; charge and discharge cut-off voltage: 5.3 and 3.0 V. The insets plot the variation in the capacities upon cycling; total charge: □; total discharge: ■; 5 V discharge: ▲; 4 V discharge: ▼. The total, 5 and 4 V capacities correspond to the capacities of 5.3–3.0 V, 5.3–4.4 V and 4.4–3.0 V, respectively.

Acknowledgements

The authors wish to thank Professor Ohoyama at Tohoku University for his skilled assistance during ND measurements, and Dr Usami at KEK for technical support of XAFS measurements. We are grateful to Dr Y. Arachi for providing us with a good sample of $ZnFe_2O_4$.

References

1 R. J. Gummow, A de Kock and M. M. Thackeray, *Solid State Ionics*, 1994, **69**, 59.
2 L. Guohua, H. Ikuta, T. Uchida and M. Wakihara, *J. Electrochem. Soc.*, 1996, **143**, 178.
3 C. Sigala, D. Guyomard, A. Verbaere, Y. Piffard and M. Tournoux, *Solid State Ionics*, 1995, **81**, 167.
4 H. Kawai, M. Nagata, M. Tabuchi, H. Tsukamoto and A. R. West, *Chem. Mater.*, 1998, **10**, 3266.
5 H. Kawai, M. Nagata, H. Kageyama, H. Tsukamoto and A. R. West, *Electrochim. Acta*, 1999, **45**, 315.
6 K. Amine, H. Tukamoto, H. Yasuda and Y. Fujita, *J. Power Sources*, 1997, **68**, 604.
7 Y. Ein-Eli, W. F. Howard, S. H. Lu, S. Mukerjee, J. Mcbeen, J. T. Vaughey and M. M. Thackeray, *J. Electrochem. Soc.*, 1998, **145**, 1238.
8 H. Shigemura, H. Sakaebe, H. Kageyama, H. Kobayashi, A. R. West, R. Kanno, S. Morimoto, S. Nasu and M. Tabuchi, *J. Electrochem. Soc.*, 2001, **148**, A730.
9 K. Oikawa, T. Kamiyama, F. Izumi, D. Nakazato, H. Ikuta and M. Wakihara, *J. Solid State Chem.*, 1999, **146**, 322.
10 P. Strobel, I. Palos and C. Bougerol, Abstract of Lithium Battery Discussion, 2001, no.16.
11 P. Aitchison, B. Ammundsen, D. J. Jones, G. Burns and J. Roziere, *J. Mater. Chem.*, 1999, **9**, 3125.
12 B. Ammundsen, D. J. Jones, J. Roziere and F. Villain, *J. Phys. Chem. B*, 1998, **102**, 7939.
13 Y. Terada, K. Yasaka, F. Nishikawa, T. Konishi, M. Yoshio and I. Nakai, *J. Solid State Chem.*, 2001, **156**, 286.
14 K. Ohoyama, T. Kanouchi, K. Nemoto, M. Ohashi, T. Kajitani and Y. Yamaguchi, *Jpn. J. Appl. Phys*, 1998, **37**, 3319.
15 F. Izumi, in *The Rietveld Method*, R. A. Young, ed., Oxford University Press, Oxford, 1993, ch. 13.
16 S. I. Zabinsky, J. J. Rehr, A. Ankudinov, R. C. Albers and M. J. Eller, *Phys. Rev. B*, 1995, **52**, 2995.
17 M. Tabuchi, K. Ado, H. Kobayashi, I. Matsubara, H. Kageyama,

M. Wakita, S. Tsutsui, S. Nasu, Y. Takeda, C. Masquelier, A. Hirano and R. Kanno, *J. Solid State Chem.*, 1998, **141**, 554.
18 M. Tabuchi, S. Tsutsui, C. Masquelier, R. Kanno, K. Ado, I. Matsubara, S. Nasu and H. Kageyama, *J. Solid State Chem.*, 1998, **140**, 159.
19 M. Tabuchi, K. Ado, H. Kobayashi, H. Sakaebe, H. Kageyama, C. Masquelier, M. Yonemura, A. Hirano and R. Kanno, *J. Mater. Chem.*, 1999, **9**, 199.
20 B. Ammundsen, D. J. Jone and J. Rosiere, *J. Solid State Chem.*, 1998, **141**, 294.
21 Y. Arachi, T. Asai, M. Nagai, Y. Katoh and M. Tabuchi, *J. Jpn Soc. Powder Powder Metall.*, 2001, **48**, 274, in Japanese.
22 R. D. Shannon, *Acta Crystallogr., Sect. A*, 1976, **32**, 751.
23 K. Kundig, M. Kobelt, H. Appel, G. Costabaris and R. H. Lindquist, *J. Phys. Chem. Solids*, 1969, **30**, 819.
24 B. Boucher, R. Buhl, R. di Bella and M. Perrin, *J. Phys. (Paris)*, 1970, **31**, 113.
25 C. Masquelier, M. Tabuchi, K. Ado, R. Kannno, Y. Kobayashi, Y. Maki, O. Nakamura and J. B. Goodenough, *J. Solid State Chem.*, 1996, **123**, 255.
26 Y. Uchimoto and T. Yao, *Abstract of International Meeting of Lithium Batteries*, 2000, no. 242.
27 T. Ozuku, K. Ariyoshi, S. Takeda and Y. Sakai, *Electrochim. Acta*, 2001, **46**, 2327.
28 Y. Gao and J. R. Dahn, *J. Solid State Ionics*, 1996, **84**, 33.
29 J. Sugiyama, T. Atsumi, A. Koiwai, T. Sasaki, T. Hioki, S. Noda and N. Kamegashira, *J. Phys.: Condens. Matter*, 1997, **9**, 1729.
30 C. Sigala, D. Guyomard, J. L. Mansot, D. Guymard, Y. Piffard and M. Tournoux, *J. Solid State Chem.*, 1997, **132**, 372.